ACS APPLIED MATERIALS & INTERFACES

Research Article

Cite This: ACS Appl. Mater. Interfaces 2019, 11, 23083−23092

www.acsami.org

Tunable Three-Dimensional Plasmonic Arrays for Large Near-Infrared Fluorescence Enhancement

Jing S. Pang,[†,∥] Ioannis G. Theodorou,[†,‡,∥] Anthony Centeno,[†,§] Peter K. Petrov,[†] Neil M. Alford,[†] Mary P. Ryan,[†] and Fang Xie*[,†]

[†]Department of Materials and London Centre for Nanotechnology, Imperial College London, SW7 2AZ, London, U.K.

[‡]Cancer Biophysics Laboratory, Department of Mechanical and Manufacturing Engineering, University of Cyprus, 40 Macedonias Avenue, Latsia 2238, Cyprus

[§]Department of Electrical and Electronic Engineering, Xi'an Jiaotong Liverpool University, 111 Ren'ai Road, Suzhou Dushu Lake Higher Education Town, Jiangsu 215123, China

Supporting Information

ABSTRACT: Metal-enhanced fluorescence (MEF), resulting from the near-field interaction of fluorophores with metallic nanostructures, has emerged as a powerful tool for dramatically improving the performance of fluorescence-based biomedical applications. Allowing for lower autofluorescence and minimal photoinduced damage, the development of multifunctional and multiplexed MEF platforms in the near-infrared (NIR) windows is particularly desirable. Here, a low-cost fabrication method based on nanosphere lithography is applied to produce tunable three-dimensional (3D) gold (Au) nanohole−disc arrays (Au-NHDAs). The arrays consist of nanoscale glass pillars atop nanoholes in a Au thin film: the top surfaces of the pillars are Au-covered (effectively nanodiscs), and small Au nanoparticles (nanodots) are located on the sidewalls of the pillars. This 3D hole−disc (and possibly nanodot) construct is critical to the properties of the device. The versatility of our approach is illustrated through the production of uniform and highly reproducible Au-NHDAs with controlled structural properties and tunable optical features in the NIR windows. Au-NHDAs allow for a very large NIR fluorescence enhancement (more than 400 times), which is attributed to the 3D plasmonic structure of the arrays that allows strong surface plasmon polariton and localized surface plasmon resonance coupling through glass nanogaps. By considering arrays with the same resonance peak and the same nanodisc separation distance, we show that the enhancement factor varies with nanodisc diameter. Using computational electromagnetic modeling, the electric field enhancement at 790 nm was calculated to provide insights into excitation enhancement, which occurs due to an increase in the intensity of the electric field. Fluorescence lifetime measurements indicate that the total fluorescence enhancement may depend on controlling excitation enhancement and therefore the array morphology. Our findings provide important insights into the mechanism of MEF from 3D plasmonic arrays and establish a low-cost versatile approach that could pave the way for novel NIR-MEF bioapplications.

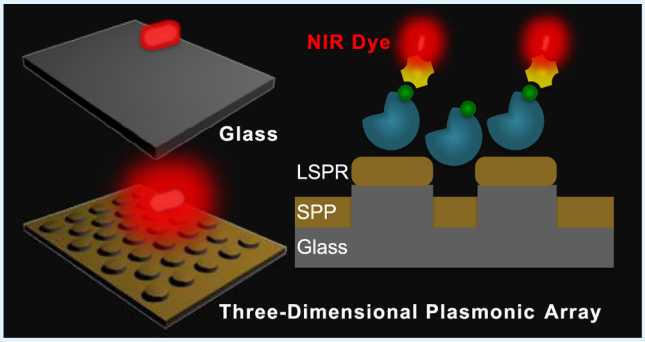

KEYWORDS: *plasmonic arrays, gold nanodiscs, near-infrared, metal-enhanced fluorescence, SPP, LSPR, nanosphere lithography*

INTRODUCTION

Metal-enhanced fluorescence (MEF) is an optical process in which the near-field interaction of fluorophores with metallic nanoparticles can, under certain conditions, lead to large fluorescence enhancement.[1−4] MEF has specifically attracted considerable interest for fluorescence-based biomedical applications,[1] such as DNA[5,6] and RNA[7] sensing, immunoassays,[8,9] or fluorescence-based imaging.[10−12] For such bioapplications, fluorophores emitting in the near-infrared (NIR: 650−900 nm) and second near-infrared (NIR-II: 1.0−1.7 μm) windows are of particular importance,[13−15] since low absorption of light by water and hemoglobin at these wavelengths allows high transparency for potential tissue imaging.[16] Meanwhile, low autofluorescence from organic molecules enables higher signal-to-noise ratio compared to that of the visible range,[17] while diminished photon scattering allows higher tissue penetration in the NIR-II window. Because of the extremely low quantum yields (QYs) of currently available NIR/NIR-II fluorophores, as well as the reduced quantum efficiencies of detectors/cameras in this wavelength range, MEF platforms for large fluorescence enhancement in the NIR/NIR-II windows are extremely desirable, as they

Received: May 21, 2019
Accepted: June 6, 2019
Published: June 6, 2019

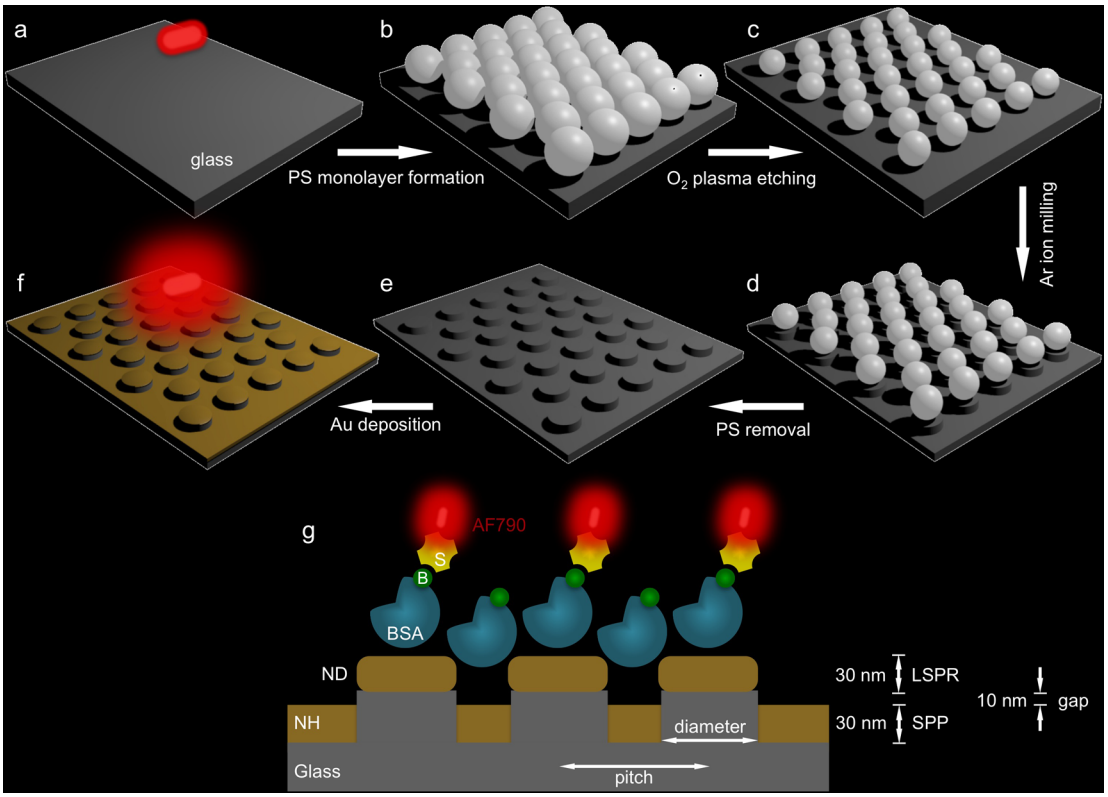

Figure 1. (a–f) Schematic workflow for the fabrication of three-dimensional (3D) gold nanohole–nanodisc arrays (Au-NHDAs) through nanosphere lithography (PS: polystyrene spheres). The Au-NHDAs are efficient platforms for near-infrared metal-enhanced fluorescence, allowing more than 400 times fluorescence enhancement. The enhancement factors are tunable through the nanoscale control of the arrays' structural characteristics. (g) Cross section of a Au-NHDA, showing the nanodiscs (NDs) deposited on the surface of the glass nanopillars and the nanohole array (NH) formed on the base of the pillars. Fluorescence enhancement was measured by immobilizing monolayers of a streptavidin (S)-functionalized near-infrared dye (AlexaFluor 790: AF790) with self-assembled monolayers of biotin (B)-labeled bovine serum albumin (BSA) through biotin–avidin binding. Schematic not to scale.

would significantly impact the applicability of such systems, resulting in greater detection sensitivity. MEF platforms with tunable optical properties and enhancement factors would be exceptionally attractive, allowing the development of novel multicolor and multiplexed sensing or imaging applications.

For MEF to occur, fluorophores need to be positioned in close proximity to the surface of metallic nanostructures (typically in the range of ~5–30 nm).[18] One of the main contributions to MEF is the significant enhancement of the local electric field close to the metal particles, which relies on the generation of a propagating surface plasmon polariton (SPP) or the localized surface plasmon resonance (LSPR). LSPR occurs when the dimensions of a metallic nanostructure are lower than the wavelength of the incident light, leading to collective but nonpropagating oscillations of surface electrons in the metallic nanostructure. In contrast, SPPs are propagating charge oscillations on the surface of thin metal films but cannot be excited by free-space radiation; instead, they require a momentum matching, such as through periodicity in a nanostructure, for resonance excitation. In addition to the electric field enhancement, the close proximity of the metal nanoparticles leads to electromagnetic coupling between the fluorescent emitter and the nanoparticle. This will modify the radiative decay rates, change the fluorescence lifetime and quantum yield, and improve the photostability of the fluorophore.[19] The magnitude of fluorescence enhancement critically depends on the design of plasmonic substrates.[20−24] Most of the traditional and commonly used MEF substrate architectures have been solely based on the local electric field enhancement from the sharp edges of nanostructures or the small gaps between them, in either porous metallic films,[9] ordered nanoparticle arrays,[2,4,23,24] or nanoparticles randomly deposited on a surface through self-assembly.[25] For instance, in our previous work, two-dimensional (2D) hexagonal arrays of Au or Ag nanoparticles (triangular[23,24] or cylindrical[4] cross sections) allowed NIR enhancement factors of up to 2 orders of magnitude. These arrays were fabricated by nanosphere lithography (NSL), which is a low-cost method that allows the production of regular arrays over large surface areas (in the order of 2 × 2 cm^2) with flexible tuning parameters. Unfortunately, MEF excitation enhancement is due to the electric field enhancement. One problem with the 2D arrays previously used is that large field enhancement is localized to "hot spots", which can be sparsely distributed over the array surface.

Recently, three-dimensional (3D) arrays fabricated by nanoimprint lithography have been reported, in which nanodiscs (LSPR mode) were located on the top of glass nanopillars situated above nanoholes in a Au thin film (SPP mode), with Au nanodots on the sidewalls of the pillars.[26] That work revealed that SPP–LSPR coupling through the glass nanogaps in such 3D structures allowed for very large fluorescence enhancement, which was uniform over large sample areas. This uniformity led to an extensive improvement in the detection sensitivity and dynamic range for protein biomarker detection using a fluorescent immunoassay.

DOI: 10.1021/acsami.9b08802
ACS Appl. Mater. Interfaces 2019, 11, 23083−23092

However, the structural characteristics and optical response of the arrays presented were not tunable.[26] Furthermore, in nanoimprint lithography, the template used to stamp the desired structure relies on other lithography techniques to be fabricated; therefore, the mask is expensive to produce and lacks the adaptability for generating a variety of shapes and structures.

In the present work, the low-cost fabrication method based on NSL previously used for 2D arrays of nanotriangles/nanodiscs[4,23,24] is extended to manufacture tunable 3D Au plasmonic structures. They consist of a nanodisc array raised above the nanoholes in a Au thin film. The fabrication steps of the Au nanohole−disc arrays (Au-NHDAs) are depicted schematically in Figure 1. We demonstrate that this protocol is capable of producing uniform and highly reproducible Au-NHDAs with exquisitely tunable structural properties, illustrating the versatility of this approach. In contrast to previous reports where a single array structure with a defined optical response was presented,[26] we show Au-NHDAs with tunable optical features in the NIR/NIR-II windows. Two such arrays are selected for maximum spectral overlap with a commercially available NIR dye (AlexaFluor 790, Abs 782 nm/Em 805 nm) to investigate whether LSPR−SPP coupling in these arrays could result in higher MEF.

To consider the effect of the nanodisc diameter on fluorescence enhancement, the arrays have the same resonance peak and the same separation distance between nanodiscs (280 nm) but different nanodisc diameters (215 nm: Au-NHDA-215 and 148 nm: Au-NHDA-148). More than 400 times enhancement is achieved with Au-NHDAs, which varies with the nanodisc diameter. Computational electromagnetic modeling offers insights into the excitation enhancement induced by the electric field enhancement. Fluorescence lifetime measurements indicate that the total fluorescence enhancement may depend on controlling the excitation enhancement and therefore the array morphology. Our findings provide important insights into the mechanism of MEF from 3D plasmonic arrays and establish a low-cost versatile approach that could pave the way for multiplexed and multicolor NIR-MEF bioapplications.

EXPERIMENTAL SECTION

Materials. Monodisperse surfactant-free polystyrene (PS) spheres (10% w/v) with diameters of 280, 400, 500, and 620 nm were purchased from Bangs Laboratories, Inc. Streptavidin-conjugated AlexaFluor 790 (AF790) was purchased from Life Technologies, UK. Phosphate-buffered saline (PBS; pH 7.4) and biotin-labeled bovine serum albumin (bBSA) were obtained from Sigma-Aldrich, UK. Low-doped p-type silicon wafers were purchased from Si-Mat, Germany. Microscope glass slides were purchased from VWR, UK. Deionized (DI) water purified using the Millipore Milli-Q gradient system (>18.2 MΩ) was used in all of the experiments.

Gold Nanohole/Disc Array (Au-NHDA) Synthesis and Characterization. Microscope glass slides (~10 × 10 mm) (Figure 1a) were cleaned using piranha solution (3:1 concentrated H_2SO_4:30% H_2O_2), at 80 °C for 1 h. Substrates were thoroughly rinsed with DI water, sonicated for 60 min in a 5:1:1 H_2O:NH_4OH:30% H_2O_2 solution, rinsed again with DI water, and used immediately. Substrates were coated with a 10 nm Ni layer by thermal evaporation using a Mantis e-beam evaporation system. The Ni thickness was controlled by the deposition monitor quartz crystal microbalance of the system. This Ni coating served as a sacrificial layer to enable complete removal of PS during the Au-NHDA synthesis, allowing a clean patterned surface to be obtained, free from PS residue that would otherwise affect the morphology of the Au arrays.

To prepare PS monolayer templates on the substrates (Figure 1b), PS spheres were first diluted with ethanol absolute in a 1:1 ratio. Aliquots of the diluted PS solutions (~3−5 μL) were applied onto the surface of a large (~30 × 20 mm) silicon wafer, which had been cleaned as above and kept in a 10% sodium dodecyl sulfate solution for 24 h. The silicon wafer was slowly submerged in a glass container filled with ~150 mL of DI water. Following submersion of the silicon substrate in water, the PS spheres formed a disordered monolayer on the water surface. Addition of a 2% sodium dodecyl sulfate solution (~4 μL), which changed the water surface tension, allowed large monolayers with highly ordered areas to be obtained. These monolayers were collected from the water surface using the Ni-coated glass/silicon substrates. The substrates were left to dry in an ambient atmosphere at approximately 30° to facilitate further self-assembly of PS on the substrate surface while drying. The diameter of PS spheres was then reduced to the required size using the oxygen plasma treatment (100 W) of controlled duration (Figure 1c).[4]

Next, substrate areas not protected by the PS mask were etched by Ar ion milling (Figure 1d), using an IM150 Oxford Applied Research ion milling system. A neutralized Ar ion beam with an energy of 500 eV and a current density of 0.2 mA/cm^2 was used to bombard the sample, which was attached to a water-cooled stage with rotation and tilting capabilities. The angular stage of the system is adjustable from 0° (normal incidence) to 45° to enable milling of three-dimensional (3D) nanostructures, while stage rotation promotes uniform ion milling of the samples.

The PS mask and the Ni sacrificial layer were removed by immersing the substrates in 10% H_2SO_4 for 5 min, generating periodic nonmetal (glass/silicon) nanopillar arrays with tunable pitches and diameters and ~40 nm height (Figure 1e). Finally, the nanopillar arrays were coated with 30 nm Au by thermal evaporation (Figure 1f), resulting in Au-NHDA, consisting of a Au backplane on the base of the pillars (nanohole array) and Au discs on top of each pillar (nanodisc array).

The morphology of the Au-NHDAs was characterized by scanning electron microscopy (SEM) using a Zeiss Auriga field emission gun SEM (FEG-SEM). SEM images were obtained on glass substrates to retain the actual geometry and morphology of the plasmonic arrays. Their optical properties were characterized using an Agilent Cary 5000 UV−vis−NIR spectrophotometer using clean glass slides as reference.

Fluorophore Attachment and Fluorescence Measurements. Dye monolayers were formed on the Au-NHDAs and glass substrates, as a control, as depicted schematically in Figure 1g. First, monolayers of bBSA on Au-NHDAs or clean glass substrates were formed by adding a 100 mg/mL solution of bBSA in PBS (50 mM, pH 7.2) onto the surface of the substrates. The substrates were incubated in a humidified atmosphere for 1 h and rinsed with PBS several times to remove unbound proteins. The substrates were then incubated for 2 h with 25 μg/mL of streptavidin-conjugated AlexaFluor 790 (AF790), to allow binding of the fluorophore to the bBSA monolayer, through avidin−biotin interaction. The samples were again rinsed with PBS several times to remove unbound fluorophores.

The fluorescence emission spectra of AF790 on Au-NHDA arrays or glass controls were collected using a Fluorolog Tau-3 system (HORIBA Jobin Yvon) with a 450 W Xe lamp excitation. All of the spectra were acquired using unpolarized light, corrected from the spectral response, and long-pass filters were used to eliminate the contribution from the scattered excitation light.

The fluorescence decay curves of AF790 were measured using the time-correlated single photon counting (TCSPC) technique,[27] using a FluoTime200 spectrometer (PicoQuant), equipped with a TimeHarp300 TCSPC board (PicoQuant) and a Hamamatsu photomultiplier (PMA-185). The excitation source was a 730 nm picosecond pulsed diode laser (PicoQuant, LDH730), driven by a PDL800-D driver (PicoQuant) and operated at a 40 MHz pulse repetition rate. Emission was collected at right angles relative to the excitation laser beam. The emission arm was fitted with a long-pass

DOI: 10.1021/acsami.9b08802
ACS Appl. Mater. Interfaces 2019, 11, 23083−23092

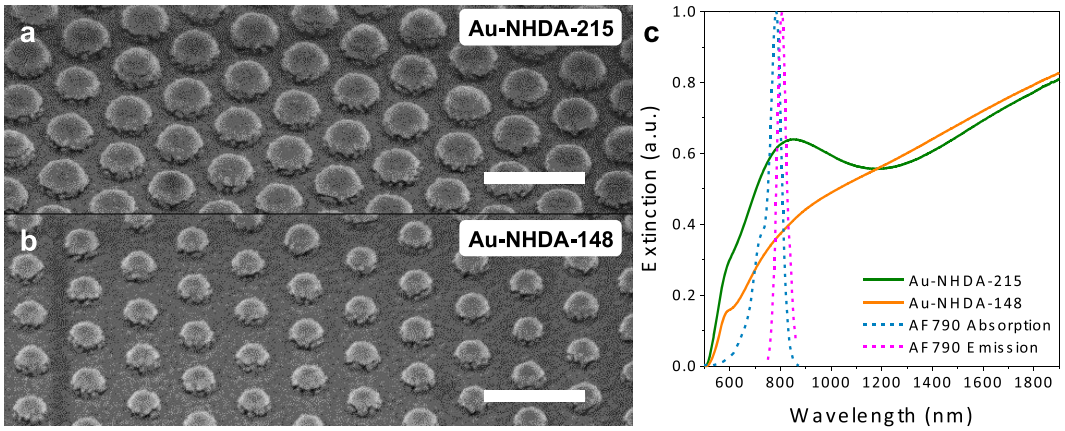

Figure 2. (a,b) Scanning electron microscopy (SEM) images of Au-NHDAs fabricated through nanosphere lithography using 280 nm polystyrene (PS) spheres, with nanodisc diameters of 215 nm (Au-NHDA-215) (a) and 148 nm (Au-NHDA-148) (b). Scale bar 400 nm. (c) Normalized extinction spectra of Au-NHDA-215 and Au-NHDA-148 (solid lines), and absorption and emission spectra of AlexaFluor 790 (AF790; dashed lines).

filter (HQ460LP, Chroma) before the monochromator (Scientech 9030). The full width at half-maximum (FWHM) of the system's instrument response function (IRF) was 350 ps. The fluorescence decay curves were analyzed using the FluoFit software (PicoQuant, version 4.2.1) based on a multiexponential model, which involves an iterative reconvolution process. The quality of the fits was assessed by the value of the reduced χ^2-value and a visual inspection of the distribution of the weighted residuals and their autocorrelation function.[28]

Computational Electromagnetic Modeling. Calculations of the electromagnetic properties of the Au-NHDAs were carried out using the finite-difference time-domain (FDTD) technique.[29] In brief, a 3D total-field scheme was used with a grid resolution of 1−2 nm in each direction. The grid resolution for each case was obtained by convergence testing. The dielectric function of Au was modeled with a Drude−Lorentz model (data provided in the Supporting Information),[30] and the glass had a dielectric constant of 2.32. To prevent nonphysical reflections from the extremities of the FDTD workspace, perfectly matched layers (PMLs) were placed at the upper and lower boundaries of the FDTD workspace. To simulate an infinite nanohole/disc array, the other boundaries had periodic boundary conditions. All FDTD calculations were carried out using the open-source MEEP FDTD code[31] on an HP Z800 workstation with two Quad core processors and 64 GB RAM. The reflections from the array, transmission into the glass and material absorption, were calculated using the method described previously,[32] where the incident field and the total field are found through surfaces in the glass and above the array.

RESULTS AND DISCUSSION

Three-Dimensional (3D) Au-NHDAs by Nanosphere Lithography with Tunable Structures and Optical Properties. Figure 2a,b shows two examples of the 3D Au-NHDAs fabricated through our newly developed protocol, and their properties are summarized in Table 1. The Au-NHDAs had a pitch (center-to-center distance) of 280 nm, while the nanodisc diameters were 215 nm (Au-NHDA-215; Figure 2a) and 148 nm (Au-NHDA-148; Figure 2b).

To obtain high-quality Au-NHDAs, several steps of the fabrication protocol were optimized to achieve a well-controlled and tunable process. First, nanosphere lithography combined with O_2 plasma etching and Ar ion milling was used to generate glass or silicon substrates patterned with hexagonal arrays of nanopillars (Figure 1e). The pitch of these arrays could be controlled by the initial PS size, while the nanopillar diameter was determined by the duration of O_2 plasma

Table 1. Structural Parameters (As Defined Schematically in Figure 1g) and Extinction Peak Positions of Au-NHDAs, and Fluorescence Enhancement Factors (E_f) for AF790

array	pitch size (nm)	diameter (nm)	gap (nm)	extinction peak (nm)	E_f (AF790)
Au-NHDA-148	280	148 ± 3	10	848	298
Au-NHDA-215	280	215 ± 5	10	848	411

etching, as well as the parameters used in the Ar ion milling (angle of milling, flux, accelerating voltage, and screen voltage). A novel approach in Ar ion milling was established to ensure that the nanopillar substrate had vertical sidewalls (Figure S1),[33] an essential requirement to guarantee that the metal nanodiscs were isolated from the underlying nanohole array, for successful LSPR and SPP couplings. For arrays with a pitch lower than 400 nm, like the ones shown in Figure 2a, the milling depth was set at 40 nm as this was the maximum depth that allowed vertical sidewalls to be maintained. Furthermore, a Ni sacrificial layer was added between the substrate and PS mask to enable complete PS removal and obtain nanopillar surfaces that were smooth and free of PS residue (Figure S1), which could have severely compromised the morphology of the final Au-NHDAs.

Following the production of the nanopillar-patterned substrates, Au deposition led to the formation of Au nanohole and nanodisc arrays on the base and top of the nanopillars, respectively. To provide a gap of approximately 10 nm between the nanodisc and nanohole arrays, 30 nm of Au was deposited on the patterned substrate. This gap distance was selected as it has been previously suggested as the optimal distance for LSPR and SPP couplings to take place.[26] In addition, we found that the deposition of 30 nm thick Au layers produced arrays with optical properties in the NIR/NIR-II windows, making them suitable for biological applications. Nonetheless, the straightforward control of the etching depth/metal deposition thickness, and therefore separation distance, through our method, could easily allow further optimization of the arrays' performance in the future.

Close inspection of the gaps between nanodiscs and nanoholes revealed the presence of small Au nanoparticles (NPs). These NPs may originate from Au deposited on the pillar sidewalls that is much thinner than that on top of the

DOI: 10.1021/acsami.9b08802
ACS Appl. Mater. Interfaces 2019, 11, 23083−23092

nanopillars. The thin Au layer is unstable and diffuses at the elevated evaporation temperature, self-assembling into small NPs.[26] Previous publications have suggested that these small metallic NPs may be an important feature of the Au-NHDAs, for example, by strongly focusing light to small regions and significantly enhancing local electric fields.[26,34] However, as the size of these small NPs was not tunable under the fabrication protocol currently used, and establishing an accurate size distribution was not possible under the current imaging conditions, their effect on fluorescence enhancement was not investigated further in the present work and remains to be evaluated. In summary, the Au-NHDA arrays produced were uniform and highly reproducible. A range of the arrays with different pitch sizes and different nanodisc diameters are shown in Figure S2, showcasing the flexibility and tunability of our developed protocol.

Overall, our protocol was able to generate Au-NHDAs with tunable optical features in the NIR/NIR-II windows. These optical properties could allow Au-NHDAs to be spectrally coupled with several different fluorophores throughout the NIR/NIR-II, which could be crucial for the development of multiplexed and multicolor biosensing applications. The extinction spectra of Au-NHDA-215 and Au-NHDA-148 are presented in Figure 2c. These arrays were selected to provide maximum spectral overlap with a commercially available NIR dye (AlexaFluor 790, Abs 782 nm/Em 805 nm; Figure 2c). An AlexaFluor dye was selected because, compared with other available dyes with similar excitation/emission, it is hydrophilic, more photostable, and less pH-sensitive, making it suitable for biosensing applications and for cell and tissue labeling.[35] In addition, this dye has a very low quantum yield (~4%) and was therefore used to test the potential of Au-NHDAs for increasing its emission efficiency. Au-NHDA-215 had a resonance peak of around 848 nm (Figure 2b), while Au-NHDA-148 did not show a clearly visible peak but the first-derivative calculation revealed a small peak also around 848 nm (Figure S3). This is in agreement with the FDTD results, discussed in the section Computational Electromagnetic Modeling, which show that the resonance peak is almost the same for both types of substrates. In the case of isolated nanodiscs of different diameters, we would expect LSPR wavelength to vary with size. However, because the nanodiscs are in hexagonal arrays, the proximity of the adjacent particles will affect the electromagnetic interaction between individual nanodiscs, as well as between nanodiscs and the Au film. The optical extinction in this array is therefore a complex function, not only of particle size but also of coupling between the particles (interparticle coupling) and coupling between particles and the Au thin film.[36−40] For fluorescence enhancement studies, we investigated two arrays with the same resonance peak, fixed pitch size, Au layer thickness, and separation gap to be able to consider the influence of the nanodisc diameter on fluorescence enhancement.

NIR Fluorescence Enhancement with Tunable Enhancement Factors. We then proceeded to test whether the Au-NHDAs fabricated through colloidal lithography could achieve high fluorescence enhancement by exploiting LSPR−SPP coupling. The potential for NIR-enhanced fluorescence was tested by immobilizing AF790 monolayers on the Au-NHDAs, using bare glass substrates as a control. Dye monolayers were formed through biotin−avidin binding of the streptavidin-functionalized dye with self-assembled monolayers of biotin-labeled bovine serum albumin (bBSA) on the Au-NHDAs and glass substrates, as depicted schematically in Figure 1g and discussed in detail in our previous work.[2,4,25] Following substrate incubation with bBSA, bBSA is expected to form complete monolayers on both glass and Au-NHDA substrates, as it is known to bind to both glass and Au surfaces: on glass, through noncovalent physisorption, while, on Au, through coordinative interaction between gold and the bBSA thiol groups.[41−43] We have previously quantified the amount of bBSA bound to glass and Au surfaces by measuring its absorbance at 280 nm and shown that, under the incubation protocol used, this amount was roughly equal between the two types of surfaces (at most 1.2 times higher on Au rather than on glass).[25] In addition, in practical biosensing applications, the fluorescent signal is measured per acquisition area regardless of the number of attached fluorophores; therefore, the uncorrected fluorescence enhancement factors are presented here, which may be more relevant.

The size of bBSA, which has an ellipsoidal shape with axes of 4 and 8 nm, combined with the streptavidin diameter of ~4 nm, provides a total spacing of ~12 nm between the dye molecules and the Au surface. The magnitude of MEF is known to be strongly dependent on dye−metal nanostructure separation distance.[32] Since electromagnetic field intensity decreases with increasing distance from the metal surface, fluorescence enhancement also decreases. On the other hand, nonradiative decay is inversely proportional to the third power of this spacing and is known to dominate at very small distances (<4 nm), consequently resulting in fluorescence quenching.[44,45] Therefore, the approach employed here using the streptavidin−biotin conjugate enables a significantly larger spacing of ~12 nm, ensuring that nonradiative decay channels are minimized.[24]

The fluorescence emission of AF790 bound to glass substrates or Au-NHDAs was measured using an excitation of 760 nm over three different areas on each substrate. The averaged emission is shown in Figure 3. Glass substrates coated with bBSA were used for background correction. The area-averaged fluorescence enhancement factors (E_f) were calculated as previously described,[24] using

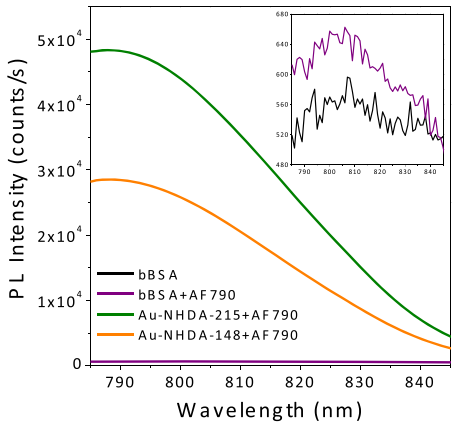

Figure 3. Photoluminescence (PL) emission spectra of streptavidin-conjugated AF790 monolayers formed on biotinylated bovine serum albumin (bBSA)-coated glass slides, Au-NHDA-215 and Au-NHDA-148. The inset shows the PL emission of AF790 on bBSA-coated glass compared to that on bare (i.e., with no fluorophore) bBSA-coated glass slides, used for background correction.

DOI: 10.1021/acsami.9b08802
ACS Appl. Mater. Interfaces 2019, 11, 23083−23092

$$E_f = \frac{I_{AF790/Au-NHDA} - I_{bBSA/Au-NHDA}}{I_{AF790/glass} - I_{bBSA/glass}} \cdot \frac{A_{uncovered}}{A_{total}} \quad (1)$$

where $I_{AF790/Au-NHDA}$ is the fluorescence intensity of AF790 on the Au-NHDAs, $I_{AF790/glass}$ is the fluorescence intensity of AF790 on glass, $I_{bBSA/Au-NHDA}$ is the background fluorescence of bBSA on the Au-NHDA, $I_{bBSA/glass}$ is the background fluorescence of bBSA on glass, $A_{uncovered}$ is the surface area of uncovered bare glass on a substrate, and A_{total} is the total surface area of the substrate. The calculated fluorescence enhancement factors (E_f) are displayed in Table 1, showing significant NIR fluorescence enhancement from both samples. MEF is a complex coupling process between fluorophores and metal nanostructures[24,32] and is usually attributed to the combined contribution of excitation and emission enhancement. Local electric field enhancements, generated close to metal nanostructures by SPP or LSPR, can result in increased excitation rates for fluorophores, leading to excitation enhancement. Emission enhancement arises from the modification of the radiative and nonradiative decay rates of nearby fluorophores by metal nanostructures, resulting in modified fluorescence lifetimes and quantum yields. Experimental and theoretical work has identified several factors that may influence the magnitude of fluorescence enhancement, including particle size, shape, interparticle separation, the surrounding dielectric medium, as well as the particle arrangement geometry and distance between the metal and fluorophore.[22,32,44] Moreover, MEF critically depends on the overlap between the LSPR in metal nanostructures and the spectral properties of the fluorophore.

As shown in Table 1, Au-NHDAs led to enhancement factors of up to 411 times. This value is lower than the 7400-fold enhancement previously reported for a similar 3D plasmonic structure,[26] possibly due to a combination of factors like the different measurement setup used or the lower spacer thickness (~6.5 nm). Nevertheless, fluorescence enhancement was significantly higher than that previously obtained by our group with Au nanodisc or Au nanotriangular arrays, under identical experimental setup conditions.[4,24] For instance, we have previously shown that for Au nanodisc arrays on glass substrates, a maximum enhancement factor of 235 times was measured with 256 nm nanodiscs for AlexaFluor 750 (Abs 749 nm/Em 775 nm) and decreased with decreasing nanodisc diameter.[4] We have also measured up to 83 times fluorescence enhancement for AF790 using Ag nanotriangular arrays (i.e., arrays of bow-tie assemblies).[24] In these 2D plasmonic arrays, coupled LSPRs arise due to the strong near-field coupling between the constitutive particles, leading to local enhancements of the electric field in the gaps between particles. This results in higher excitation rates for fluorophores positioned close to these electric field "hot spots", leading to MEF through excitation enhancement. In the 2D plasmonic arrays previously explored, however, "hot spots" may be sparsely distributed over the array surface, limiting large fluorescence enhancement only to confined regions of the array. In our 3D plasmonic Au-NHDAs in contrast, apart from interparticle coupling, SPP−LSPR coupling could result in electric field enhancements that are more uniform over larger surface areas, thus resulting in the higher overall MEF measured here. Although the SPP effect in nanohole arrays typically results in weaker electric field enhancements compared to LSPR, their convolution in the Au-NHDAs through the nanogaps results in a much stronger field concentration through coupling.[26] Previous work on Ag nanocap−nanohole pairs, for instance, has shown that the electric field enhancement was sensitive to the size of the gap.[46] As previously suggested, the 3D array may be extremely efficient in receiving excitation light and radiating fluorescent light.[26] It has been proposed, for example, that the small gaps in the array structure and the small metallic dots located on the sidewalls of the glass nanopillars may be able to strongly focus light onto small regions and significantly enhance the local electric fields.[26,34] Consequently, in contrast to the large proportion of exposed bare glass areas in nanodisc or nanotriangular arrays, the high density of nanodiscs, gaps, and dots in Au-NHDAs leads to a higher percentage of fluorophores near areas of electric field hot spots, hence increasing the average fluorescence enhancement. This enhancement has already been shown to dramatically improve the sensitivity and dynamic range for protein biomarker detection in fluorescent immunoassays.[26] Here, the tunability of the enhancement factors was achieved, with higher fluorescence enhancement measured for Au-NHDA-215 compared to that for Au-NHDA-148. We believe this is likely due to the shorter distance between individual nanodiscs leading to stronger LSPR interparticle coupling, which is consistent with the previously reported work.[4,23,24] Therefore, the protocol presented here for Au-NHDA fabrication may be a significant step forward in the application of MEF in biomedical applications as it allows straightforward control of the arrays' structural properties, in contrast to nanoimprint lithography, which lacks the flexibility in producing different structures using the same mask. The ability to produce arrays with tunable enhancement factors and therefore tune the sensitivity of detection to different concentrations of biomarkers of interest in a single sample is crucial for the future development of multiplexed detection platforms.

In addition, the excitation angle and polarization could play important roles in determining the resonance mode in our LSPR−SPP coupled system.[47−49] The ability to tune the plasmonic mode, and consequently fluorescence emission, could be useful for a wide range of bioimaging and biosensing applications. As a first attempt to examine the effect of the excitation angle, we measured the fluorescence enhancement factors for AF790 at 30 and 45° (Table S1). Our data showed that, by increasing the excitation angle to 45°, there was around 10% increase in the enhancement factor of Au-NHDA-148 but a slight decrease in the case of Au-NHDA-215. These findings suggest that MEF using our Au-NHDAs may indeed be sensitive to the excitation angle, which will be explored in detail in the future to further optimize our arrays' performance.

In contrast to our previous work on nanodisc and nanotriangular arrays,[4,23,24] where fluorescence emission intensity was stable throughout the experiments, considerable intensity decrease was observed during the acquisition process with the Au-NHDAs. For instance, the first measurement of emission intensity of AF790 using Au-NHDA-215 showed an enhancement factor of 505 times, degrading to 411 when measured 30 min later. To verify that this was not caused by the measurement setup, the fluorescence intensity from AF790 on bare glass substrates was measured and was steady throughout 3 h of measurements. Therefore, for consistency, fluorescence measurements for all samples (i.e., values in Table 1) were collected 30 min after the first exposure to the excitation light source. Consequently, the enhancement factors presented here are semiquantitative and are a lower estimation of the full potential of the Au-NHDAs for fluorescence

DOI: 10.1021/acsami.9b08802
ACS Appl. Mater. Interfaces 2019, 11, 23083−23092

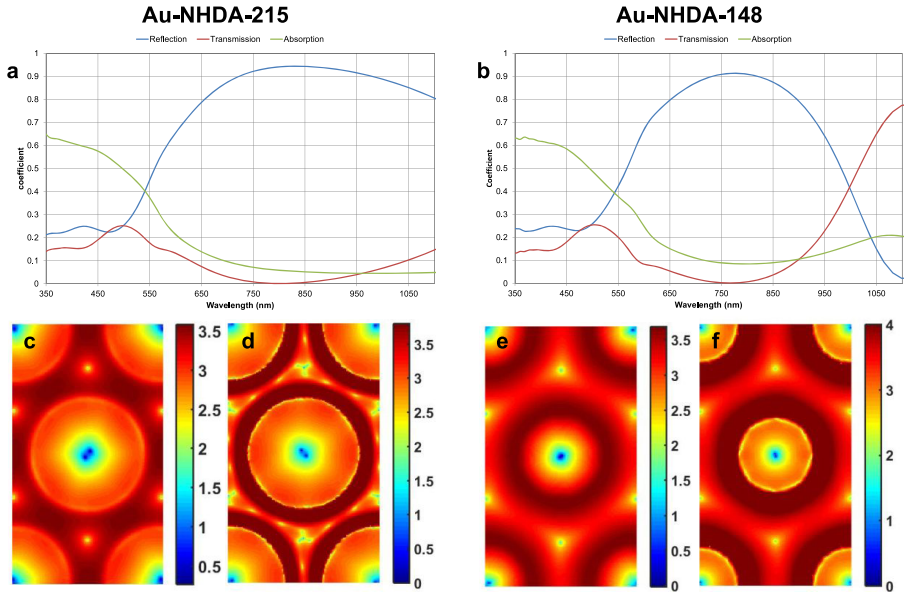

Figure 4. Spectral response (reflection, transmission, and absorption) (a,b) and **E** field enhancement ($\mathbf{E}/\mathbf{E}_i$) (c–f; logarithmic scale) calculated with three-dimensional (3D) finite-difference time-domain (FDTD) modeling for Au-NHDA-215 (a,c,d) and Au-NHDA-148 (b,e,f). The **E** field enhancement was calculated 12 nm above the surface of the Au nanodiscs (c,e) or 12 nm above the Au thin-film surface (d,f), for a 790 nm incident wave.

enhancement, since a proportion of the fluorophores had been degraded over the measurement period. This is an interesting observation, as it is generally accepted that MEF improves the photostability of fluorophores, by decreasing their lifetime and therefore allowing a greater excitation/emission cycle rate.[50] However, as discussed in the section Computational Electromagnetic Modeling, the electric field enhancement is very high for the arrays reported here, about 2 orders of magnitude higher than that previously reported by our group, especially near the surface of the nanodiscs. We speculate that the photobleaching observed may be caused by an intersystem crossing for a small number of fluorophore in regions of an extremely high electric field, which is consistent with the previous work.[51] We therefore expect that there is a finite number of fluorophores on the substrate affected, after which the system is stable. This observation also suggests that there may be a maximum field enhancement that should be designed into this system.

Computational Electromagnetic Modeling. For computational calculations, we considered arrays with the same properties of those measured experimentally (Figure 2 and Table 1) and as depicted schematically in Figure 1g. Figure 4a,b shows the calculated reflection, transmission, and absorption spectra for Au-NHDA-148 and Au-NHDA-215. In both cases, transmission minima are observed at wavelengths between 750 and 800 nm. For Au-NHDA-148, absorption minima and reflection maxima appear at wavelengths close to the transmission minima. For Au-NHDA-215, the calculated absorption continues to decline with increasing wavelength and a local minimum is not observed close to the transmission minimum. Nevertheless, for both samples, significant features in the spectral response are observed close to the excitation and emission wavelengths of AF790.

In MEF, excitation enhancement occurs due to an increase in the intensity of the electric field. Therefore, to draw further insights into the mechanism of fluorescence enhancement, the electric field enhancement at 790 nm was calculated for both samples. The results, for a distance of 12 nm above the surface of either the Au nanodiscs (Figure 4c,e) or the Au thin film (Figure 4d,f), are shown in Figure 4. This height was selected to directly correspond to the estimated total spacing of ∼12 nm between the dye molecules and the Au-NHDA surface provided by the bBSA–streptavidin spacer used in our experiments. If the surface area of high field enhancement available for fluorophore attachment was considered, a higher fluorescent enhancement due to increased excitation would be expected with the Au-NHDA-148. Still, the field enhancements obtained by our modeling results (Figure 4c–f) are quite similar between the two types of Au-NHDAs, which corresponds to the similar enhancement factors measured through our fluorescence measurements (Figure 3). In addition, our model did not take into account the small metallic NPs located in the sidewalls of the nanopillars, which may be an important feature of the arrays, possibly able to significantly enhance local electric fields.

The electromagnetic field modeling data also suggest that the excitation enhancement, due to the increased electric field, should be approaching or even exceeding 3 orders of magnitude; therefore, the actual fluorescent enhancement measured is lower than expected. A possible explanation for this observation could be the absorption of fluorophore emissions by the Au surfaces. As shown in our previous work using Au spheres,[32] only fluorophore emissions that are normal to the surface of the sphere will be enhanced. Here, emissions with field components that are normal to the nanocylinder will be tangential to the Au film. Since the metal is not a perfect conductor at this wavelength, there will be some absorption of the emitted field causing a reduction in the emission enhancement. Therefore, further investigation in this area is required to optimize the array geometry for higher-emission enhancement.

Fluorescence Lifetime Measurements. Further insights into the respective contributions of excitation and emission enhancement to the total enhancement factors were obtained

DOI: 10.1021/acsami.9b08802
ACS Appl. Mater. Interfaces 2019, 11, 23083–23092

from fluorescence lifetime measurements. This also enabled us to estimate the modification of the fluorophore's quantum yield by the Au-NHDAs.[52] The fluorescence lifetime spectra of AF790 on the Au-NHDAs, as well as bare glass substrates as a control, are shown in Figure 5. To evaluate these data, we used

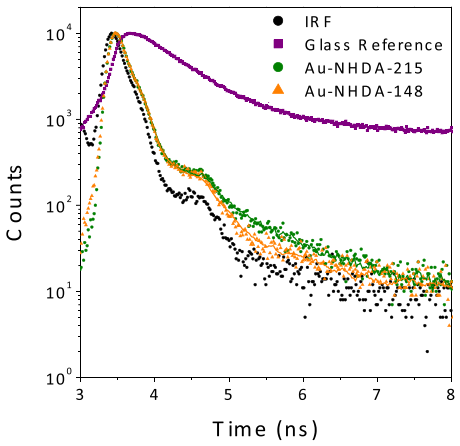

Figure 5. Fluorescence lifetime spectra of streptavidin-conjugated AF790 monolayers immobilized on Au-NHDAs and on glass substrates as a control. The dotted line shows the instrument response function (IRF).

a multiexponential (ME) model, which describes the fractional contribution of decay times of different components in a sample mixture.[53] For our data, an acceptable fitting required a model with two decay times, τ_1 and τ_2, from which an average value is calculated using the weighting a_1 and a_2

$$I(t) = a_1 \, e^{-t/\tau_1} + a_2 \, e^{-t/\tau_2} \quad (2)$$

The results of fitting to an ME decay model are summarized in Table S3. The χ^2_R values represent the goodness-of-fit parameter, obtained by fitting experimentally measured parameters to calculated values through a nonlinear least-squares deconvolution process. The average lifetime of AF790 monolayer on glass was found to be 600 ps, in agreement with our previous reports.[24,25] As shown in Figure 5, fluorescence lifetime was considerably decreased on both Au-NHDAs. However, the decreased lifetime reached the detection limit of the detector available for measurements (~50 ps). Based on the ME model fitting, we estimate that the fluorescence lifetime may have substantially decreased to values close to 20 ps for both Au-NHDAs (Table S3).

The lifetime data were then analyzed within the framework of a well-established semiempirical model,[52] as discussed in detail in our previous work.[4,25] Using the measured fluorescence lifetime of AF790 on glass and the unmodified quantum yield of AF790 (4%),[25] we estimated the modified quantum yield for each Au-NHDA and thus the emission enhancement factor (E_{em}), defined as $E_{em} = Q_m/Q_0$. Then, the excitation enhancement factor (E_{ex}) for each sample was calculated by dividing the total fluorescence enhancement factor (E_f, Table 1) by the emission enhancement ($E_{ex} = E_f/E_{em}$), as shown in Table S4. Although the values are semiquantitative due to the detection limit of the detector, they indicate that the radiative decay rate of AF790 increased significantly on Au-NHDAs, causing the quantum yield of the fluorophores to increase. The observed emission enhancement suggests that the fluorophore coupled to the SPP/LSPR generated by the Au-NHDAs. The high values of modified quantum yield estimated for AF790 on both Au-NHDAs (~97%) show that these arrays can dramatically increase the brightness of low-quantum-yield NIR dyes to levels similar to those of visible dyes. However, the fluorescence decay curves of AF790 were almost identical for both types of Au-NHDAs, probably due to the fact that both measurements are approaching the IRF. Thus, the limitations of the instrumentation used in the present study indicate that it is challenging to quantitatively determine the modified quantum yield and consequently the emission enhancement. Although further lifetime data may be required to more thoroughly characterize our system, our findings indicate that array morphology may significantly impact the mechanism of fluorescence enhancement, emphasizing the capabilities of our fabrication protocol in producing arrays with controlled structural properties to achieve tunable enhancement factors.

CONCLUSIONS

In summary, the large near-infrared fluorescence enhancement measured for Au-NHDAs fabricated by nanosphere lithography (more than 400 times) confirms that these arrays are promising NIR-MEF platforms for the development of biosensing applications, where analytes at extremely low concentrations can be detected. By considering arrays with the same pitch and resonance peak, we showed that emission enhancement was not significantly different for the nanodisc diameters considered. These findings show that the enhancement factors, and hence the sensitivity of Au-NHDAs, can be tuned by manipulating the structural characteristics of the arrays, highlighting the potential of our fabrication protocol, which is flexible to several different structures. Our findings provide insights into the mechanism of MEF from 3D plasmonic arrays that can be used to guide the future design of NIR/NIR-II biomedical applications.

ASSOCIATED CONTENT

Supporting Information

The Supporting Information is available free of charge on the ACS Publications website at DOI: 10.1021/acsami.9b08802.

Fluorescence enhancement factors (E_f) for AF790 at excitation angles of 30 and 45°, parameters used in FDTD calculations for gold, SEM image of patterned silicon substrate, SEM images of Au-NHDAs with various structures, normalized extinction spectra of Au-NHDA-215 and Au-NHDA-148 with first-derivative calculation, multiexponential analysis of intensity decay of AF790 monolayers and calculated values of modified quantum yield (Q_m), total enhancement factor (E_f), emission enhancement factor (E_{em}), and excitation enhancement factor (E_{ex}) of AF790 on Au-NHDAs (PDF)

AUTHOR INFORMATION

Corresponding Author

*E-mail: f.xie@imperial.ac.uk.

ORCID

Ioannis G. Theodorou: 0000-0002-9572-417X

Fang Xie: 0000-0001-6415-797X

Author Contributions

‖J.S.P. and I.G.T. contributed equally to this work.

DOI: 10.1021/acsami.9b08802
ACS Appl. Mater. Interfaces 2019, 11, 23083−23092

Notes

The authors declare no competing financial interest.

■ ACKNOWLEDGMENTS

I.G.T. and F.X. are supported by a British Council Newton Grant (No. 216239013). F.X. acknowledges an ICiC grant funded by MRC Confidence in Concept and the Royal Marsden NHS Foundation Trust. M.P.R. is grateful for funding via an RAEng/Shell Research Chair in Interfacial Nanoscience.

■ REFERENCES

(1) Darvill, D.; Centeno, A.; Xie, F. Plasmonic Fluorescence Enhancement by Metal Nanostructures: Shaping the Future of Bionanotechnology. *Phys. Chem. Chem. Phys.* **2013**, *15*, 15709−15726.
(2) Theodorou, I. G.; Jawad, Z. A. R.; Qin, H.; Aboagye, E. O.; Porter, A. E.; Ryan, M. P.; Xie, F. Significant Metal Enhanced Fluorescence of Ag2S Quantum Dots in the Second Near-Infrared Window. *Nanoscale* **2016**, *8*, 12869−12873.
(3) Jawad, Z. A. R.; Theodorou, I. G.; Jiao, L. R.; Xie, F. Highly Sensitive Plasmonic Detection of the Pancreatic Cancer Biomarker CA 19-9. *Sci. Rep.* **2017**, *7*, No. 14309.
(4) Pang, J.; Theodorou, I. G.; Centeno, A.; Petrov, P. K.; Alford, N. M.; Ryan, M. P.; Xie, F. Gold Nanodisc Arrays as Near Infrared Metal-Enhanced Fluorescence Platforms with Tuneable Enhancement Factors. *J. Mater. Chem. C* **2017**, *5*, 917−925.
(5) Cheng, Y.; Stakenborg, T.; Van Dorpe, P.; Lagae, L.; Wang, M.; Chen, H.; Borghs, G. Fluorescence Near Gold Nanoparticles for DNA Sensing. *Anal. Chem.* **2011**, *83*, 1307−1314.
(6) Wang, Y.; Liu, B.; Mikhailovsky, A.; Bazan, G. C. Conjugated Polyelectrolyte−Metal Nanoparticle Platforms for Optically Amplified DNA Detection. *Adv. Mater.* **2010**, *22*, 656−659.
(7) Aslan, K.; Huang, J.; Wilson, G. M.; Geddes, C. D. Metal-Enhanced Fluorescence-Based RNA Sensing. *J. Am. Chem. Soc.* **2006**, *128*, 4206−4207.
(8) Szmacinski, H.; Murtaza, Z.; Lakowicz, J. R. Time-Resolved Fluorometric Method for One-Step Immunoassays using Plasmonic Nanostructures. *J. Phys. Chem. C* **2010**, *114*, 7236−7241.
(9) Tabakman, S. M.; Lau, L.; Robinson, J. T.; Price, J.; Sherlock, S. P.; Wang, H.; Zhang, B.; Chen, Z.; Tangsombatvisit, S.; Jarrell, J. A.; Utz, P. J.; Dai, H. Plasmonic Substrates for Multiplexed Protein Microarrays with Femtomolar Sensitivity and Broad Dynamic Range. *Nat. Commun.* **2011**, *2*, No. 466.
(10) Zhang, J.; Fu, Y.; Lakowicz, J. R. Fluorescent Metal Nanoshells: Lifetime-Tunable Molecular Probes in Fluorescent Cell Imaging. *J. Phys. Chem. C* **2011**, *115*, 7255−7260.
(11) Saha, A.; Basiruddin, S. K.; Sarkar, R.; Pradhan, N.; Jana, N. R. Functionalized Plasmonic−Fluorescent Nanoparticles for Imaging and Detection. *J. Phys. Chem. C* **2009**, *113*, 18492−18498.
(12) Theodorou, I. G.; Ruenraroengsak, P.; Gonzalez-Carter, D. A.; Jiang, Q.; Yagüe, E.; Aboagye, E. O.; Coombes, R. C.; Porter, A. E.; Ryan, M. P.; Xie, F. Towards Multiplexed Near-Infrared Cellular Imaging using Gold Nanostar Arrays with Tunable Fluorescence Enhancement. *Nanoscale* **2019**, *11*, 2079−2088.
(13) Luo, S.; Zhang, E.; Su, Y.; Cheng, T.; Shi, C. A Review of NIR Dyes in Cancer Targeting and Imaging. *Biomaterials* **2011**, *32*, 7127−7138.
(14) Wan, H.; Yue, J.; Zhu, S.; Uno, T.; Zhang, X.; Yang, Q.; Yu, K.; Hong, G.; Wang, J.; Li, L.; Ma, Z.; Gao, H.; Zhong, Y.; Su, J.; Antaris, A. L.; Xia, Y.; Luo, J.; Liang, Y.; Dai, H. A Bright Organic NIR-II Nanofluorophore for Three-Dimensional Imaging into Biological Tissues. *Nat. Commun.* **2018**, *9*, No. 1171.
(15) Theodorou, I. G.; Jiang, Q.; Malms, L.; Xie, X.; Coombes, R. C.; Aboagye, E. O.; Porter, A. E.; Ryan, M. P.; Xie, F. Fluorescence Enhancement from Single Gold Nanostars: Towards Ultra-Bright Emission in the First and Second Near-Infrared Biological Windows. *Nanoscale* **2018**, *10*, 15854−15864.
(16) Weissleder, R. A Clearer Vision for In Vivo Imaging. *Nat. Biotechnol.* **2001**, *19*, 316−317.
(17) Hilderbrand, S. A.; Weissleder, R. Near-Infrared Fluorescence: Application to In Vivo Molecular Imaging. *Curr. Opin. Chem. Biol.* **2010**, *14*, 71−79.
(18) Deng, W.; Xie, F.; Baltar, H. T.; Goldys, E. M. Metal-Enhanced Fluorescence in the Life Sciences: Here, Now and Beyond. *Phys. Chem. Chem. Phys.* **2013**, *15*, 15695−15708.
(19) Xie, F.; Baker, M. S.; Goldys, E. M. Homogeneous Silver-Coated Nanoparticle Substrates for Enhanced Fluorescence Detection. *J. Phys. Chem. B* **2006**, *110*, 23085−23091.
(20) Aslan, K.; Lakowicz, J. R.; Geddes, C. D. Plasmon Light Scattering in Biology and Medicine: New Sensing Approaches, Visions and Perspectives. *Curr. Opin. Chem. Biol.* **2005**, *9*, 538−544.
(21) Lakowicz, J. R.; Ray, K.; Chowdhury, M.; Szmacinski, H.; Fu, Y.; Zhang, J.; Nowaczyk, K. Plasmon-Controlled Fluorescence: A New Paradigm in Fluorescence Spectroscopy. *Analyst* **2008**, *133*, 1308−1346.
(22) Bardhan, R.; Grady, N. K.; Cole, J. R.; Joshi, A.; Halas, N. J. Fluorescence Enhancement by Au Nanostructures: Nanoshells and Nanorods. *ACS Nano* **2009**, *3*, 744−752.
(23) Xie, F.; Centeno, A.; Ryan, M. R.; Riley, D. J.; Alford, N. M. Au Nanostructures by Colloidal Lithography: From Quenching to Extensive Fluorescence Enhancement. *J. Mater. Chem. B* **2013**, *1*, 536−543.
(24) Xie, F.; Pang, J. S.; Centeno, A.; Ryan, M. P.; Riley, D. J.; Alford, N. M. Nanoscale Control of Ag Nanostructures for Plasmonic Fluorescence Enhancement of Near-Infrared Dyes. *Nano Res.* **2013**, *6*, 496−510.
(25) Theodorou, I. G.; Jawad, Z. A. R.; Jiang, Q.; Aboagye, E. O.; Porter, A. E.; Ryan, M. P.; Xie, F. Gold Nanostar Substrates for Metal-Enhanced Fluorescence through the First and Second Near-Infrared Windows. *Chem. Mater.* **2017**, *29*, 6916−6926.
(26) Zhou, L.; Ding, F.; Chen, H.; Ding, W.; Zhang, W.; Chou, S. Y. Enhancement of Immunoassay's Fluorescence and Detection Sensitivity Using Three-Dimensional Plasmonic Nano-Antenna-Dots Array. *Anal. Chem.* **2012**, *84*, 4489−4495.
(27) Lakowicz, J. R. Radiative Decay Engineering 5: Metal-Enhanced Fluorescence and Plasmon Emission. *Anal. Biochem.* **2005**, *337*, 171−194.
(28) Danos, L.; Markvart, T. Excitation Energy Transfer Rate from Langmuir Blodgett (LB) Dye Monolayers to Silicon: Effect of Aggregate Formation. *Chem. Phys. Lett.* **2010**, *490*, 194−199.
(29) Taflove, A.; Hagness, S. C. *Computational Electrodynamics: The FDTD Method*; Artech House: Boston, London 2000.
(30) Rakić, A. D.; Djurišić, A. B.; Elazar, J. M.; Majewski, M. L. Optical Properties of Metallic Films for Vertical-Cavity Optoelectronic Devices. *Appl. Opt.* **1998**, *37*, 5271−5283.
(31) Oskooi, A. F.; Roundy, D.; Ibanescu, M.; Bermel, P.; Joannopoulos, J. D.; Johnson, S. G. Meep: A Flexible Free-Software Package for Electromagnetic Simulations by the FDTD Method. *Comput. Phys. Commun.* **2010**, *181*, 687−702.
(32) Centeno, A.; Alford, N.; Xie, F. Predicting the Fluorescent Enhancement Rate by Gold and Silver Nanospheres using Finite-Difference Time-Domain Analysis. *IET Nanobiotechnol.* **2013**, *7*, 50−58.
(33) Pang, J. S. *Engineered Nanostructures for Metal Enhanced Fluorescence Applications in the Near-Infrared*; Imperial College London: London, 2014.
(34) Li, W.-D.; Ding, F.; Hu, J.; Chou, S. Y. Three-Dimensional Cavity Nanoantenna Coupled Plasmonic Nanodots for Ultrahigh and Uniform Surface-Enhanced Raman Scattering over Large Area. *Opt. Express* **2011**, *19*, 3925−3936.
(35) Panchuk-Voloshina, N.; Haugland, R. P.; Bishop-Stewart, J.; Bhalgat, M. K.; Millard, P. J.; Mao, F.; Leung, W.-Y.; Haugland, R. P. Alexa Dyes, a Series of New Fluorescent Dyes that Yield Exceptionally Bright, Photostable Conjugates. *J. Histochem. Cytochem.* **1999**, *47*, 1179−1188.
(36) Jain, P. K.; El-Sayed, M. A. Plasmonic Coupling in Noble Metal Nanostructures. *Chem. Phys. Lett.* **2010**, *487*, 153−164.

DOI: 10.1021/acsami.9b08802
ACS Appl. Mater. Interfaces 2019, 11, 23083−23092

(37) Li, G.-C.; Zhang, Y.-L.; Lei, D. Y. Hybrid Plasmonic Gap Modes in Metal Film-Coupled Dimers and their Physical Origins Revealed by Polarization Resolved Dark Field Spectroscopy. *Nanoscale* **2016**, *8*, 7119−7126.
(38) Mock, J. J.; Hill, R. T.; Degiron, A.; Zauscher, S.; Chilkoti, A.; Smith, D. R. Distance-Dependent Plasmon Resonant Coupling between a Gold Nanoparticle and Gold Film. *Nano Lett.* **2008**, *8*, 2245−2252.
(39) Nordlander, P.; Prodan, E. Plasmon Hybridization in Nanoparticles near Metallic Surfaces. *Nano Lett.* **2004**, *4*, 2209−2213.
(40) Félidj, N.; Aubard, J.; Lévi, G.; Krenn, J. R.; Schider, G.; Leitner, A.; Aussenegg, F. R. Enhanced Substrate-Induced Coupling in Two-Dimensional Gold Nanoparticle Arrays. *Phys. Rev. B* **2002**, *66*, No. 245407.
(41) Nuzzo, R. G.; Dubois, L. H.; Allara, D. L. Fundamental Studies of Microscopic Wetting on Organic Surfaces. 1. Formation and Structural Characterization of a Self-Consistent Series of Polyfunctional Organic Monolayers. *J. Am. Chem. Soc.* **1990**, *112*, 558−569.
(42) Gustafson, T. P.; Cao, Q.; Wang, S. T.; Berezin, M. Y. Design of Irreversible Optical Nanothermometers for Thermal Ablations. *Chem. Commun.* **2013**, *49*, 680−682.
(43) Borzenkov, M.; Chirico, G.; D'Alfonso, L.; Sironi, L.; Collini, M.; Cabrini, E.; Dacarro, G.; Milanese, C.; Pallavicini, P.; Taglietti, A.; Bernhard, C.; Denat, F. Thermal and Chemical Stability of Thiol Bonding on Gold Nanostars. *Langmuir* **2015**, *31*, 8081−8091.
(44) Bharadwaj, P.; Novotny, L. Spectral Dependence of Single Molecule Fluorescence Enhancement. *Opt. Express* **2007**, *15*, 14266−14274.
(45) Centeno, A.; Xie, F.; Alford, N. Light Absorption and Field Enhancement in Two-Dimensional Arrays of Closely Spaced Silver Nanoparticles. *J. Opt. Soc. Am. B* **2011**, *28*, 325−330.
(46) Wen, X.; Xi, Z.; Jiao, X.; Yu, W.; Xue, G.; Zhang, D.; Lu, Y.; Wang, P.; Blair, S.; Ming, H. Plasmonic Coupling Effect in Ag Nanocap−Nanohole Pairs for Surface-Enhanced Raman Scattering. *Plasmonics* **2013**, *8*, 225−231.
(47) Oldenburg, S. J.; Hale, G. D.; Jackson, J. B.; Halas, N. J. Light Scattering from Dipole and Quadrupole Nanoshell Antennas. *Appl. Phys. Lett.* **1999**, *75*, 1063−1065.
(48) Lodewijks, K.; Ryken, J.; Van Roy, W.; Borghs, G.; Lagae, L.; Van Dorpe, P. Tuning the Fano Resonance Between Localized and Propagating Surface Plasmon Resonances for Refractive Index Sensing Applications. *Plasmonics* **2013**, *8*, 1379−1385.
(49) He, J.; Zheng, W.; Ligmajer, F.; Chan, C.-F.; Bao, Z.; Wong, K.-L.; Chen, X.; Hao, J.; Dai, J.; Yu, S.-F.; Lei, D. Y. Plasmonic Enhancement and Polarization Dependence of Nonlinear Upconversion Emissions from Single Gold Nanorod@SiO2@CaF2:Yb3+,Er3+ Hybrid Core−Shell−Satellite Nanostructures. *Light: Sci. Appl.* **2017**, *6*, No. e16217.
(50) Geddes, C. D.; Lakowicz, J. R. Editorial: Metal-Enhanced Fluorescence. *J. Fluoresc.* **2002**, *12*, 121−129.
(51) Galloway, C. M.; Artur, C.; Grand, J.; Le Ru, E. C. Photobleaching of Fluorophores on the Surface of Nanoantennas. *J. Phys. Chem. C* **2014**, *118*, 28820−28830.
(52) Dragan, A. I.; Geddes, C. D. Metal-enhanced fluorescence: The Role of Quantum Yield, Q0, in Enhanced Fluorescence. *Appl. Phys. Lett.* **2012**, *100*, No. 093115.
(53) Lakowicz, J. R. Time-Domain Lifetime Measurements. In *Principles of Fluorescence Spectroscopy*, 3rd ed.; Lakowicz, J. R., Ed.; Springer, 2006; pp 97−155.

DOI: 10.1021/acsami.9b08802
ACS Appl. Mater. Interfaces 2019, 11, 23083−23092